PAPER

Check for updates

Room-temperature rapid synthesis of hierarchically porous ZIF-93 for effective adsorption of volatile organic compounds†

Haiqi Zhang,[a] Kaikai Zhao,[a] Weibiao Guo,[a] Kuan Liang,[a] Jingjing Li,[a] Xu Li,[d] Qianjun Deng,[a] Xuejun Xu,[a] Huixia Chao,[c] Hongxia Xi [iD] *[b] and Chongxiong Duan [iD] *[a]

Facile synthesis conditions, abundant hierarchical porosity, and high space–time yields (STYs) are prerequisites for the commercial application of zeolitic imidazolate frameworks (ZIFs). However, these prerequisites are rarely achieved simultaneously. Herein, a green and versatile strategy to rapidly synthesize hierarchically porous ZIFs (HP-ZIFs) was developed using an alkali as a deprotonating agent. The synthesis conditions were room temperature and ambient pressure in an aqueous solution, and the synthesis time could be reduced to 1 min. The produced HP-ZIFs had hierarchically porous structures with mesopores and macropores interconnected with micropores. The STY for HP-ZIFs was up to 9670 kg m^{-3} d^{-1}, at least 712 times the previously reported values. In addition, the porosity and morphology of the produced HP-ZIFs could be fine-tuned by controlling the synthesis parameters (*e.g.*, reaction time, molar ratios, metal source, and alkali source). Compared with conventional ZIFs, the adsorption performance of the as-synthesized HP-ZIFs for *p*-xylene and *n*-hexane was significantly improved. Positron annihilation lifetime spectroscopy (PALS) was utilized to study the pore properties, and the adsorption behavior of HP-ZIFs on guest molecules was investigated using density functional theory (DFT) simulations. This strategy shows significant promise for the large-scale industrial production of desirable HP-ZIFs for adsorption applications.

1 Introduction

Hierarchically porous zeolitic imidazolate frameworks (HP-ZIFs) are tetrahedral topological crystalline materials with zeolite-like structures.[1,2] Compared with conventional zeolitic imidazolate frameworks (ZIFs) with only micropores (pore size < 2 nm), HP-ZIFs possess hierarchically porous structures with micropores, mesopores (pore size: 2–50 nm) and/or macropores (pore size > 50 nm).[3] The mesopores and/or macropores introduced into ZIFs effectively facilitate the diffusion rate and reduce the mass-transfer resistance of guest molecules, especially large molecules (*e.g.*, volatile organic compounds (VOCs)[4]). Additionally, the generated mesopores and/or macropores will increase the total pore volume and expose more active sites, improving the internal environment of ZIFs. Therefore, the specific advantages of hierarchical pores endow HP-ZIF great potential for various applications such as adsorption/separation,[5,6] environmental remediation,[7,8] biomedicine,[9,10] and catalysts.[11,12]

To date, many effective and trustworthy strategies, including ligand extension,[13,14] template,[15,16] post-modification,[17,18] mixed-ligands,[19,20] and modulator induction methods,[21,22] have been developed to synthesize HP-ZIFs. Although these methods successfully prepared HP-ZIFs with desirable structures, they involve high temperature and pressure conditions for solvothermal synthesis using significant amounts of energy and organic solvents, thus generating large energy waste and environmental pollution. Consequently, developing green synthetic routes to reduce

[a] *School of Materials and Energy, Foshan University, Foshan, 528231, P. R. China. E-mail: cechxduan@fosu.edu.cn*
[b] *School of Chemistry and Chemical Engineering, South China University of Technology, Guangzhou, 510640, P. R. China. E-mail: cehxxi@scut.edu.cn*
[c] *Guangxi Key Laboratory of Green Chemical Materials and Safety Technology, College of Petroleum and Chemical Engineering, Beibu Gulf University, Qinzhou, 535011, P. R. China*
[d] *Key Laboratory of Nuclear Solid-State Physics Hubei Province, School of Physics and Technology, Wuhan University, Wuhan 430072, P. R. China*
† Electronic supplementary information (ESI) available. See DOI: https://doi.org/10.1039/d4im00033a

© 2025 The Author(s). Co-published by the Institute of Process Engineering, Chinese Academy of Sciences and the Royal Society of Chemistry

Ind. Chem. Mater., 2025, **3**, 109–121 | **109**

the use of toxic and expensive organic solvents, employing cheap and safe green solvents (*e.g.*, H_2O), or even utilizing solvent-free synthesis, and minimizing energy wastage are essential for the industrial production of HP-ZIFs.[23–25] Recently, Ramos-Fernandez *et al.*[26,27] utilized Zamak (Zn alloy) residues as a zinc source for the production of ZIF-8 for the first time under solvent-free conditions. Although this method successfully avoided the use of organic solvents, the synthesis process required high temperatures to melt the reactants, which is not in line with green chemistry principles. Additionally, the as-synthesized ZIF-8 was not a pure phase and contained unreacted Zamak powder, necessitating further processing to enhance its purity. Furthermore, the as-synthesized ZIF-8 did not exhibit a hierarchical pore structure. In contrast, Yu *et al.*[28] synthesized nanoscale hierarchically porous ZIF-67 using a milder room-temperature water-based method with *N,N*-dimethyl ethylenediamine as a templating agent. The presence of hierarchical pores resulted in ZIF-67 exhibiting stronger adsorption and catalytic properties. Although they successfully synthesized HP-ZIFs with hierarchically porous structures using green solvents, the process inevitably involved organic templating agents. These organic templating agents are toxic and difficult to completely remove during synthesis, which may significantly affect the pore properties of HP-ZIFs and thus limit their performance in various applications.

This study developed a rapid, water-based strategy to synthesize hierarchically porous ZIF-93 (ZIF-93_A*t*) within 1 min using an alkali as an inorganic deprotonating agent at room temperature. The resulting ZIF-93_A*t* displayed a hierarchically porous structure comprising micropores, mesopores, and macropores. Furthermore, a possible deprotonation mechanism during the synthesis of ZIF-93_A*t* was investigated. The synthetic route is highly versatile, as other inorganic bases (*e.g.*, KOH and $NH_3 \cdot H_2O$) and other zinc salts (*e.g.*, $Zn(NO_3)_2$ and $ZnSO_4$) can also be used to synthesize hierarchically porous ZIF-93. The highest space–time yield (STY) of HP-ZIF-93 was up to 9670 kg m^{-3} d^{-1}, at

least 712 times higher than previously reported values.[29] Additionally, ZIF-93_A1 was applied to adsorb VOCs (*p*-xylene and *n*-hexane), and its adsorption performance was significantly higher than that of conventional ZIF-93.

2 Results and discussion

2.1 Composition, microstructure and stability of hierarchically porous ZIF-93

The powder XRD patterns of the as-synthesized ZIF-93_A*t* (*t* = 1, 10, 60) were compared with the conventional ZIF-93 (C-ZIF-93) and simulated patterns from Materials Studio package 5.0 to verify the crystal structures of ZIF-93_A*t*. As shown in Fig. 1a, the diffraction peaks of the ZIF-93_A*t*, C-ZIF-93, and the simulated data were consistent, indicating that highly crystalline ZIF-93 was obtained. In addition, the intensity of the ZIF-93_A*t* peaks increased as the reaction time increased from 1 to 60 min, which could be attributed to an increased crystallinity.[30] Furthermore, the ZIF-93_A*t* composition was verified using the FT-IR spectral analysis. As shown in Fig. 1b, the FT-IR spectra of the ZIF-93_A*t* samples were consistent with that of C-ZIF-93. The broad peak at 3290–3720 cm^{-1} is generated by O–H stretching vibration. The sharp peak at 2844 cm^{-1} is generated by the hydrogen stretching vibration of the aldehyde group. The peaks in the range of 600–1700 cm^{-1} originate from the 4-methylimidazole-5-carbaldehyde (almeIm) in the structure of ZIF-93.[31–35] The characteristic peak for Zn–N is 570 cm^{-1}.[36,37] XRD and FT-IR have combined to confirm the successful formation of ZIF-93 crystals and to verify the pure phase of ZIF-93_A*t*.

SEM and TEM were used to investigate the morphology and porosity of the ZIF-93 samples. As shown in Fig. 2, SEM image shows that the ZIF-93_A1 crystal particles are more uniformly distributed, and the average diameter is about 278 nm. With the prolongation of the reaction time, the average diameter of the ZIF-93_A*t* crystal particles increases, and non-uniformity of the particle size was observed. In particular, ZIF-93_A60 has a particle size distribution
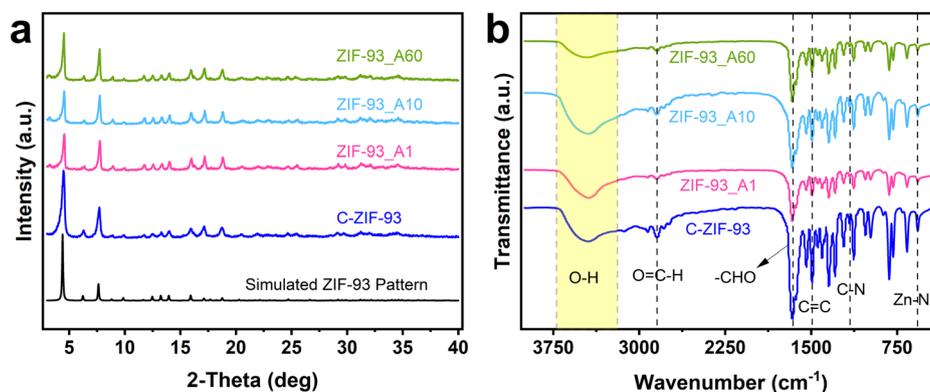

Fig. 1 (a) Powder XRD patterns of ZIF-93_A*t* (*t* = 1, 10, 60) and C-ZIF-93 samples and simulated XRD pattern of ZIF-93. (b) FT-IR spectra of the as-synthesized ZIF-93_A*t* (*t* = 1, 10, 60) and C-ZIF-93.
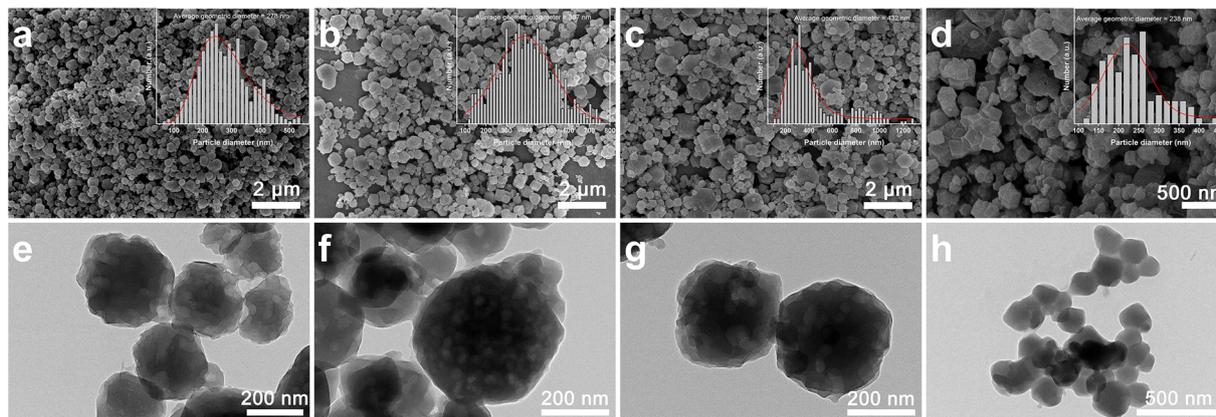
Fig. 2 SEM and TEM images of ZIF-93 samples: (a and e) ZIF-93_A1, (b and f) ZIF-93_A10, (c and g) ZIF-93_A60, and (d and h) C–ZIF-93.

spanning the nanometer to micrometer scale. This is mainly due to the continuous nucleation of new particles as the reaction time increases and the continued growth of the crystals that nucleate first. In contrast, the crystal particles of C-ZIF-93 appeared to be twinned, and the average diameter of the single crystals was 238 nm, whereas the actual twin size was much larger than that of the single crystals. TEM image shows that the ZIF-93_At crystal has defects on the surface and abundant pores inside. These defects and pores are attributed to the corrosive effect of alkali. Furthermore, the stacking between small particles forms abundant stacking pores.[38,39] C-ZIF-93, on the other hand, exhibits obvious twinning phenomenon, and the crystal surface is very smooth with no obvious internal pores. Due to the high symmetry, ZIFs are highly susceptible to crystal twinning during nucleation.[40] Since the solvothermal method used for C-ZIF-93 lacks external influence during the synthesis, the crystals can grow freely. In contrast, ZIF-93_At is less prone to form twins during the synthesis due to the use of external stirring. The elemental distribution diagram of ZIF-93_At showed uniform dispersion of C, O, N, and Zn throughout

the crystal, as shown in Fig. 3. The specific elemental contents are shown in Table S1 and Fig. S1,† respectively. The results indicate that the chemical composition and chemical state of the surface elements were almost unchanged when introducing the hierarchically porous structures.

The thermal stability of the ZIF-93_At samples were evaluated by TGA under the N$_2$ atmosphere. As shown in Fig. S2,† the as-synthesized ZIF-93_At and C-ZIF-93 samples exhibited a similar weight loss trend during the same thermal treatment. Specifically, three primary stages of weight loss were observed. The initial weight loss in the temperature range of 30–100 °C could be attributed to the evaporation of the trapped solvents (methanol and deionized water),[41] indicating that the samples dried under vacuum at room temperature had residual solvents and a more stringent drying method, such as heating the sample below the thermal decomposition in a vacuum oven could be used. The second step of the weight loss in the temperature range of 100–400 °C may be because the guest molecule (almeIm) trapped in the pore or framework was removed.[42] The main loss occurred after 400 °C, which was the onset of the
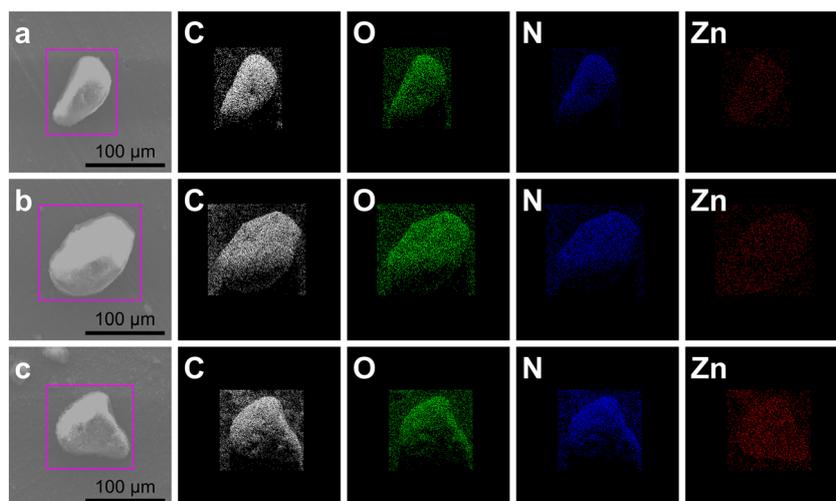

Fig. 3 Elemental distribution maps of ZIF-93_At: (a) ZIF-93_A1, (b) ZIF-93_A10, and (c) ZIF-93_A60.

thermal decomposition and the structural breakdown of ZIF-93 crystals.[43–45] In addition, the as-synthesized ZIF-93_A1 maintained its intrinsic crystal structure after soaking it in water for three months, whereas C-ZIF-93 exhibited a few degenerations, as confirmed by powder XRD patterns (Fig. S3†). These results indicate that the as-synthesized ZIF-93_At crystals have excellent thermal stability and water stability.

2.2 Porosities of hierarchically porous ZIF-93

N_2 adsorption–desorption isotherms and pore size distributions (PSDs, calculated by density functional theory (DFT)) were used to investigate the porosity properties of ZIF-93. As shown in Fig. 4a, according to the definition of IUPAC,[3] ZIF-93_At and C-ZIF-93 exhibited the distinctive characteristics of type I and IV(a) isotherms. The type I isotherm is characterized by a rapid increase in adsorption at very low pressures ($P/P_0 < 0.02$), which was attributed to the interaction of N_2 with the narrow micropores (<2 nm), resulting in rapid filling of the micropores. The N_2 adsorption at low pressure increased with increasing reaction time, suggesting that the increase in reaction time leads to more micropores in ZIF-93. Type IV(a) isotherm is characterized by a rapid rise in adsorption at lower relative pressures, a convex isotherm and an inflection point indicate the completion of monolayer adsorption. As the pressure increases, multilayer adsorption occurs. Upon desorption, a clear H4-type hysteresis loop appeared, which was attributed to the capillary coalescence phenomenon occurring in the mesopores, indicating the presence of slit mesopores in ZIF-93. In addition, ZIF-93_At samples had significantly larger hysteresis loops than C-ZIF-93. More information on the porosities of ZIF-93 was obtained from the PSDs. As shown in Fig. 4b, other than the inherent micropores and small mesopores (<5 nm), the as-synthesized ZIF-93_At contained a large number of pores with a wide 10–150 nm PSD, while C-ZIF-93 exhibited fewer mesopores and macropores than ZIF-93_A1 and ZIF-93_A10. These results indicate the successful introduction of larger mesopores and macropores in ZIF-93 crystal.

The pore-related data of ZIF-93_At and C-ZIF-93 samples was summarized in Table 1. All ZIF-93_At samples had almost equal BET specific surface area (S_{BET}). However, the total pore volume (V_t), mesopore volume (V_{meso}), and pore size of ZIF-93_At increased with decreased synthesis time, indicating that shorter reaction times could result in more and larger pores. The reason for the increase in mesopores mainly driven from stacked pores. The different reaction times resulted in different particle sizes of ZIF-93_At. The particles synthesized within 1 min have a more homogeneous size distribution and are smaller in size, and it is easier to form dense stacks between small particles, which are rich in mesopores. As the reaction time increases, the crystals that nucleate first continue to grow to form larger crystals, resulting in particles that are less likely to stack with each other, and therefore fewer stacked mesopores are formed. Compared with ZIF-93_At, C-ZIF-93 has a larger V_{micro} and a smaller V_{meso}. This is mainly due to the differences in the synthesis process. Specifically, C-ZIF-93 avoided alkali corrosion during the synthesis process, thus maximizing the retention of micropores in its structure, whereas mesopores were relatively few. In addition, the crystal morphology of C-ZIF-93 is dominated by twins. Twin crystals have a larger particle size compared to single crystals. Due to the larger particle size and specific crystal arrangement of the twins, it is difficult to stack to form an obvious mesoporous structure.

N_2 adsorption–desorption measurement is a commonly used method to characterize porosity. However, the N_2 adsorption method also has obvious disadvantages that make it difficult to distinguish the microporous structure.[46,47] Therefore, in order to obtain more accurate microporous data for hierarchically porous ZIF-93, CO_2 adsorption tests were performed on ZIF-93_A1 at 273 K. As shown in Fig. S4a,† the CO_2 adsorption–desorption isotherms exhibited a huge hysteresis loop and the desorption isotherms appeared to be non-closed. This may be due to the large electrostatic adsorption of CO_2 by the aldehyde group in the ligand of ZIF-93, resulting in the failure of CO_2 desorption completely. The microporous pore size distribution plot (Fig. S4b†) further showed that the micropores of ZIF-93_A1 were mainly
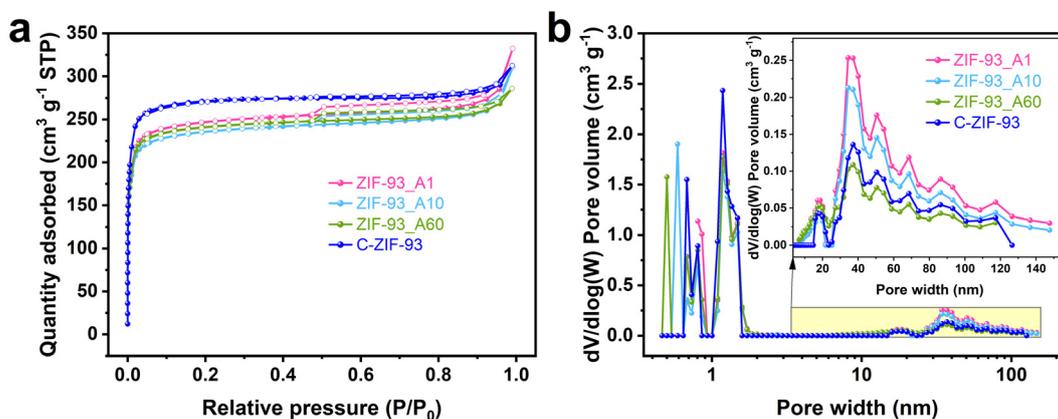

Fig. 4 (a) N_2 adsorption–desorption isotherms and (b) pore size distributions of ZIF-93_At and C-ZIF-93 samples.

Table 1 Porosity properties of the ZIF-93_At (t = 1, 10, 60) and C-ZIF-93 samples

Samples	Synthesis time	S_{BET}[a] [m^2 g^{-1}]	S_{micro}[b] [m^2 g^{-1}]	S_{ext}[c] [m^2 g^{-1}]	V_t[d] [cm^3 g^{-1}]	V_{micro}[e] [cm^3 g^{-1}]	V_{meso}[f] [cm^3 g^{-1}]	Pore size[g] [nm]	STYs[h] [kg m^{-3} d^{-1}]
ZIF-93_A1	1 min	991	863	128	0.51	0.32	0.19	6.6	3570
ZIF-93_A10	10 min	943	819	124	0.47	0.31	0.16	6.0	406
ZIF-93_A60	60 min	973	861	112	0.44	0.32	0.12	4.6	72
C-ZIF-93	12 h	1097	999	98	0.48	0.38	0.10	5.2	49

[a] S_{BET}: Brunauer–Emmett–Teller (BET) surface area. [b] S_{micro}: micropore surface area based on t-plot method. [c] S_{ext}: external surface area based on t-plot method. [d] V_t: single point adsorption total pore volume of pores. [e] V_{micro}: micropore volume based on t-plot method. [f] V_{meso}: total pore volume minus microporous pore volume. [g] Pore size: BJH desorption average pore width. [h] STYs: space–time yields calculated based on the mass of active products (equation in ESI†).

distributed in the range of 0.4–0.7 nm. Calculations performed using the Dubinin–Radushkevich method[48] have determined a micropore volume of 0.18 cm^3 g^{-1} and an equivalent surface area of 455 m^2 g^{-1}. Additionally, the median pore width, as calculated by the Horvath–Kawazoe method,[49] was found to be 0.40 nm.

2.3 Other factors that may affect the structure of hierarchically porous ZIF-93

One of the attractive features of ZIFs is the porosity properties. Since synthetic ZIFs usually have guest molecules (*e.g.*, solvents, unreacted organic ligands, clusters, *etc.*) trapped in the pore channels, it is often necessary to remove the guest molecules through an activation process to enhance the surface area and pore volume of the material.[50,51] However, the activation process often uses organic solvents (*e.g.*, acetone, methanol, and methylene chloride) and is performed at high temperatures, inevitably generating more pollution and energy waste. Therefore, this study compared the activation and non-activation effects on hierarchically porous ZIF-93 and discussed if activation was necessary for the synthesis method proposed. As shown in Fig. S5,† the characterization results showed that the XRD pattern and characteristic peaks in the FT-IR spectra for the activated ZIF-93 were consistent with the results of the fresh ZIF-93. Furthermore, SEM and TEM images of the activated and fresh ZIF-93 showed similar crystal sizes and clear mesopores and macropores (Fig. S6†). TGA curves showed that all samples had good thermal stability (Fig. S7†). In addition, N$_2$ adsorption–desorption isotherms and PSDs indicate that all ZIF-93 samples have micropores, mesopores and macropores (Fig. S8†). However, the activated ZIF-93 exhibited more micropores and a few macropores. Furthermore, Table S2† showed that the relevant surface area and porosity the two materials were not significantly different. These results indicate that activation did not enhance the surface area and pore properties of ZIF-93_At substantially.

In addition, the effect of different zinc salts on the synthesis of hierarchically porous ZIF-93 was investigated to prove the universality of the proposed method. Different zinc salts (Zn(NO$_3$)$_2$ and ZnSO$_4$) were selected based on the synthesis method of this study, and ZIF-93_Zn(NO$_3$)$_2$ and ZIF-93_ZnSO$_4$ were the hierarchically porous ZIF-93 synthesized successfully within 1 min. As shown in Fig. S9,† all characteristic peak positions in the XRD patterns of the as-synthesized ZIF-93_Zn(NO$_3$)$_2$ and ZIF-93_ZnSO$_4$ were identical to those of ZIF-93_At and C-ZIF-93. The FT-IR spectra showed consistent peak positions for the three ZIF-93 samples, confirming that Zn(NO$_3$)$_2$ and ZnSO$_4$ could be used as zinc sources for the synthesized ZIF-93 crystals. SEM and TEM images showed the crystal morphology and pore structure of all ZIF-93 samples. As shown in Fig. S10,† the crystal morphology and size distribution of ZIF-93 synthesized with Zn(OAc)$_2$ and Zn(NO$_3$)$_2$ are almost similar, the crystal surfaces are all very rough, and the particle sizes are all about 270 nm. In contrast, the crystal of ZIF-93 synthesized using ZnSO$_4$ exhibits a very regular dodecahedron and has a relatively larger crystal size of 780 nm. The TGA curves showed that the three samples had essentially the same weight loss phases (Fig. S11†), demonstrating good thermal stability. N$_2$ adsorption–desorption isotherms showed that the three ZIF-93 samples exhibited a combination of type I and IV(a) isotherms with clear hysteresis loops (Fig. S12a†), demonstrating that they had hierarchically porous structures. At low pressures (P/P_0 < 0.02), ZIF-93_A1 and ZIF-93_Zn(NO$_3$)$_2$ had the highest and lowest adsorption, respectively. Furthermore, PSDs showed that the three ZIF-93 samples had hierarchically porous structures (Fig. S12b†), and ZIF-93_Zn(NO$_3$)$_2$ had the most mesopores (40–120 nm). As shown in Table S2,† ZIF-93_Zn(NO$_3$)$_2$ and ZIF-93_ZnSO$_4$ samples had the smallest S_{BET} and V_t. However, the pore size of ZIF-93 synthesized using both Zn(NO$_3$)$_2$ and ZnSO$_4$ was about 8 nm, which was larger than that of ZIF-93 synthesized using Zn(OAc)$_2$.

In addition, hierarchically porous ZIF-93 samples were successfully synthesized using different alkalis (NH$_3$·H$_2$O and KOH) within 1 min (denoted as ZIF-93_NH$_3$·H$_2$O and ZIF-93_KOH, respectively). The XRD patterns and FT-IR spectra of the as-synthesized ZIF-93_NH$_3$·H$_2$O and ZIF-93_KOH agreed with the results of ZIF-93_A1 (Fig. S13†), proving that the as-synthesized crystals were ZIF-93 crystals. SEM and TEM images (Fig. S14†) showed that none of the

three ZIF-93 particles had a defined morphology, which could be attributed to the use of $Zn(OAc)_2$ as the zinc source. The particle size of ZIF-93 synthesized using NaOH was more uniform with an average particle diameter of 278 nm, while the particle size of ZIF-93 synthesized using KOH and $NH_3 \cdot H_2O$ was not uniform with average particle diameters of 300 nm and 195 nm, respectively. TGA curves showed that all samples had good thermal stability (Fig. S15†). N_2 adsorption–desorption isotherms showed that all samples were similar to ZIF-93_A1 with a combination of type I and IV(a) isotherms with a clear hysteresis loop (Fig. S16a†), confirming the co-existence of micropores and mesopores in crystals. Meanwhile, the PSDs and porosity data (Fig. S16b and Table S2†) showed that the pore sizes of all samples spanned three ranges (micropore, mesopore, and macropore) and the maximum pore size of ZIF-93_$NH_3 \cdot H_2O$ was about 240 nm. Therefore, the results indicate that hierarchically porous ZIF-93 could be synthesized within 1 min at room temperature using different bases.

Different molar ratios of Zn^{2+}/almeIm/H_2O had significant effects on the structure and porosity properties of ZIF-93. Based on the present research, the molar ratios of Zn^{2+}/almeIm and Zn^{2+}/H_2O were changed, respectively. As shown in Fig. S17,† ZIF-93 crystals could not be formed when the molar ratio of Zn^{2+}/almeIm was 1/0.5. However, ZIF-93 was successful synthesized by increasing the amount of almeIm. This indicates that the molar ratio of Zn^{2+}/almeIm needs to be minimized, meaning that an excess of almeIm is required for the formation of ZIF-93. This was demonstrated by Liu *et al.*[52] who also synthesized high quality ZIF-93 with a Zn^{2+}/almeIm molar ratio of 1/8. On the other hand, the amount of H_2O had less effect on the crystalline structure of ZIF-93, but decreasing the amount of H_2O significantly increased the STYs (Table S2†), where the maximum STY for hierarchically porous ZIF-93 reached 9970 kg m^{-3} d^{-1} when the molar ratio of Zn^{2+}/H_2O is 1/1390. N_2 adsorption–desorption isotherms were used to study porosity properties of the samples. As shown in Fig. S18a,† the isotherm exhibits a type V, and the hysteresis loop is of the H3-type only when the molar ratio of Zn^{2+}/almeIm is 1/0.5. This indicates that these amorphous particles do not have pores in themselves, but pores formed by stacking between particles. While other ZIF-93 samples showed type I/IV(a) combined isotherms with H4-type hysteresis loops. The pore size distribution plot (Fig. S18b†) further shows that a large number of stacked mesopores exist at a molar ratio of Zn^{2+}/almeIm of 1/0.5, but these stacks form pores with limited stiffness and are not suitable for adsorption applications. Other ZIF-93 samples showed a clear distribution of micropores–mesopores–macropores. Among them, the microporous content increased with the increase of H_2O dosage. However, only when the molar ratio of Zn^{2+}/almeIm/H_2O was 1/2/2780, the distribution of micropores–mesopores–macropores was more ideal. More detailed pore data are summarized in Table S2.†

2.4 Possible mechanism for the rapid synthesis of hierarchically porous ZIF-93

To investigate the role of the inorganic base (OH^-) in the rapid room-temperature synthesis of hierarchically porous ZIF-93, the effect of pH on synthesizing hierarchically porous ZIF-93 by varying the amount of inorganic base was explored. Notably, the initial pH was 5.8, and no precipitation without inorganic base. CH_3COOH was added dropwise to the solution which became clear and yielded no solid precipitate (Fig. S19†), to lower the pH to approximately 5. Large amounts of solid precipitates were produced when different OH^- amounts were added to the solution to adjust its pH in the range of 6–10. The solid precipitates were tested at different pH levels using XRD. As shown in Fig. S20,† all of them matched the characteristic peaks of ZIF-93, indicating the formation of ZIF-93 crystal. The intensity of the characteristic XRD peaks decreased with increased pH, indicating that the crystal structure of ZIF-93 was destroyed with the increased pH. As shown in Fig. S21,† SEM images of ZIF-93 at different pH levels revealed that obvious crystal structures of the particles were observed for pH 6 or 7. However, many small amorphous particles, along with some individual larger particles with crystal structures, appeared for a pH of 8 or 9. Only small amorphous particles were observed for pH 10. Pore analysis of ZIF-93 at different pH levels was performed using N_2 adsorption–desorption isotherms and PSDs. As shown in Fig. S22a,† all ZIF-93 samples exhibited N_2 adsorption–desorption mixing isotherms of type I/IV(a). PSDs further illustrated the pore structure. As shown in Fig. S22b,† all materials had abundant hierarchically porous structures, with the most mesopores and macropores formed due to the agglomeration of their amorphous small particles at pH 9 and 10. More detailed pore data is shown in the Table S2.† Therefore, the results indicate that the inorganic bases play an important role in synthesizing hierarchically porous ZIF-93, where OH^- from bases deprotonated the organic ligand imidazole and promoted the formation of coordination bonds with Zn^{2+}.[25,53–55]

Based on the results obtained and the literature precedents, a plausible mechanism for the rapid synthesis of hierarchically porous ZIF-93 at room temperature was presented in Fig. 5. In the initial stage, metal ions (Zn^{2+}) and organic ligands (almeIm) were uniformly dispersed in the aqueous solution. Upon adding an inorganic deprotonating agent (OH^-) under rapid stirring, OH^- underwent immediate and strong interaction with almeIm, leading to its rapid deprotonation. This is the key factor that enabled the rapid crystallization of ZIF-93. Subsequently, Zn^{2+} readily coordinated with the deprotonated almeIm to form ZIF-93. Conversely, experimental findings revealed that the acid addition suppressed the deprotonation of almeIm. Notably, the OH^- deprotonation occurred randomly, resulting in different nucleation rates for each crystal and ZIF-93 with heterogeneous crystal sizes. With the aggregation of
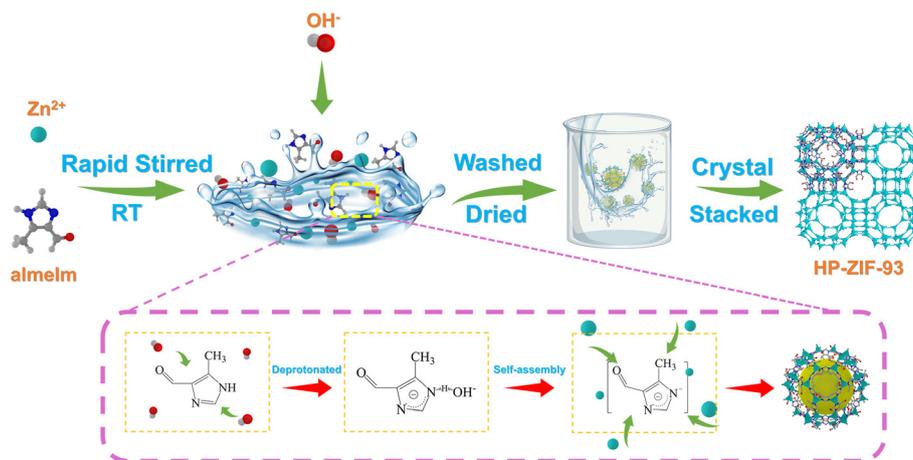
Fig. 5 A possible mechanism for the green synthesis of hierarchically porous ZIF-93.

heterogeneous crystals, abundant meso- and macropore channels are formed. Additionally, the corrosive effect of OH^- causes the ZIF-93 crystals to produce defective pores.

Energy savings, cost reduction, high safety, and increased productivity are important factors in determining the large-scale production of hierarchically porous ZIFs.[56,57] Conventional ZIF-93 requires a long reaction time at high temperatures and pressures, which leads to a large amount of energy waste and is extremely dangerous with low STY. The reaction usually uses an organic solvent with some toxicity (*e.g.*, DMF), polluting the environment.[58] Ramos-Fernandez *et al.*[29] first discovered that ZIF-93 could be synthesized at room temperature and pressure using water as a solvent, but the synthesis time was up to 18 h and STY was only 14 kg m^{-3} d^{-1}. Furthermore, the as-synthesized ZIF-93 was micron-sized without mesopores and macropores. In the synthetic strategy of this study, hierarchically porous ZIF-93 could be synthesized in an aqueous solution at room temperature and pressure, with the synthesis time reduced to only 1 min. Due to the extremely short reaction time, the STY was significantly high with a maximum of 9970 kg m^{-3} d^{-1}, which was 712 times higher than that of Ramos-Fernandez *et al.* Compared with the conventional ZIF-93, the water-based rapidly synthesized ZIF-93 also has very significant advantages in terms of STYs (Table 1). These results suggested that the proposed strategy of synthesizing hierarchically porous ZIF-93 with a green and fast synthesis method has the potential to scale up to industrial levels.

2.5 VOCs adsorption performance of hierarchically porous ZIF-93

The ZIF-93_A*t* sample was used as an adsorbent to capture VOCs (*p*-xylene and *n*-hexane). Fig. 6 shows the adsorption isotherms of ZIF-93_A1 and C-ZIF-93 for *p*-xylene and *n*-hexane at 298 K, respectively. At low relative pressure ($P/P_0 < 0.1$), all ZIF-93 exhibited a sharp increase in the uptake, which later increased slowly. ZIF-93_A1 demonstrated the highest adsorption capacities for both *p*-xylene and *n*-hexane at a relative pressure (P/P_0) of 0.9. The maximum uptakes of ZIF-93_A1 for *p*-xylene and *n*-hexane were 206 mg g^{-1} and 205 mg g^{-1}, respectively. These values were significantly higher than those of C-ZIF-93, which exhibited maximum capacities of 191 mg g^{-1} for *p*-xylene and 149 mg g^{-1} for *n*-hexane. In addition, ZIF-93_A1 was soaked in *p*-xylene and *n*-hexane for two weeks, respectively. The obtained XRD
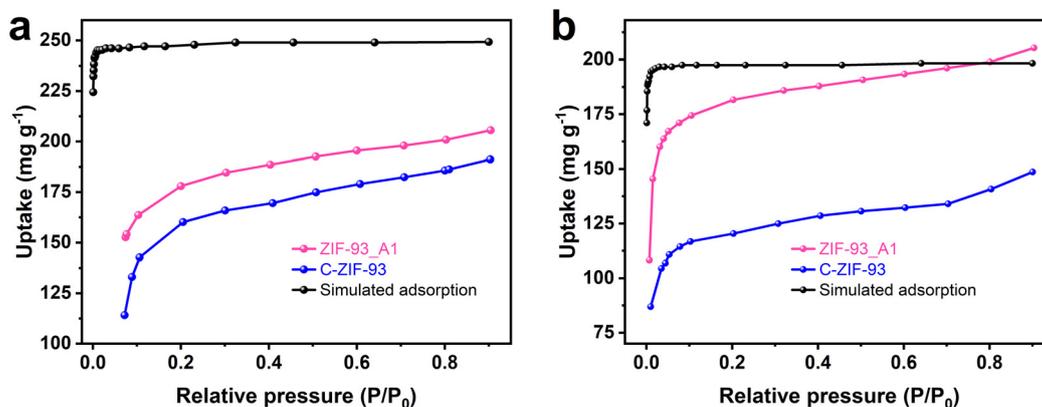

Fig. 6 Adsorption isotherms of ZIF-93_A1, C-ZIF-93 samples, and simulations at 298 K for: (a) *p*-xylene, and (b) *n*-hexane.
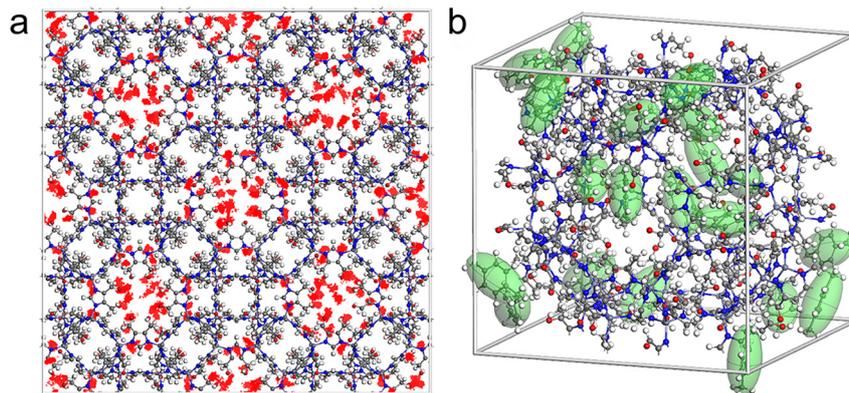
Fig. 7 (a) Adsorption density distribution and (b) adsorption distribution of *p*-xylene on ZIF-93 at a relative pressure of 0.3 (*P/P₀*).

patterns (Fig. S23†) showed that ZIF-93_A1 could still maintain its crystal structure, which proves that ZIF-93_A1 has good stability. Grand canonical Monte Carlo (GCMC) simulations were used to calculate the adsorption of ZIF-93 on *p*-xylene and *n*-hexane. The simulation results (Fig. 6) showed that the adsorption trend of the calculated results was consistent with the experimental results, and ZIF-93 exhibited enhanced adsorption performance for *p*-xylene. The kinetic diameters of *n*-hexane and *p*-xylene are 4.3 Å and 5.85 Å,[59,60] respectively, while the ZIF-93 theoretical model has a maximum channel diameter of 5.58 Å in the ⟨001⟩ direction.[61] Theoretically, *n*-hexane should more easily enter the cavity of ZIF-93, resulting in a stronger adsorption capacity. However, both experimental and simulation results showed that ZIF-93 had a stronger adsorption capacity for *p*-xylene. The reasons for this result are multifaceted. On one hand, the larger pore size facilitates the entry of both *n*-hexane and *p*-xylene into the cavity of ZIF-93. On the other hand, the adsorption distribution plots (Fig. 7 and S24†) showed that *p*-xylene and *n*-hexane were mainly dispersed around the aldehyde groups of the ligand. The aldehyde groups on the walls of the ZIF-93 pores exert strong forces on these VOCs molecules, but the nature of these interaction forces varies. While *n*-hexane forms a weak van der Waals dipole interaction with the aldehyde group, *p*-xylene forms a stronger π-π host-guest interaction.[62] The electrostatic potential distributions were calculated using density

functional theory (DFT) (Fig. 8 and S25†). The results of the interaction energies showed that the interaction energy of ZIF-93 with *p*-xylene was significantly larger than that with *n*-hexane. Thus, the results demonstrate that the presence of a hierarchical pore structure not only enables macromolecules to enter the pore space quickly, but also that the increase in pore size exposes more adsorption sites, thereby increasing the adsorption force.

2.6 Pore connectivity investigation of hierarchically porous ZIF-93

In order to further investigate the pore connectivity of ZIF-93_A1, positron annihilation lifetime spectroscopy (PALS) was performed on ZIF-93_A1 before and after adsorption of *p*-xylene. PALS is a non-destructive spectroscopic technique used to study pores and defects of solid materials. The sample is bombarded with positrons (*i.e.*, electron anti-particle) and the pore sizes are determined by the interaction of the positrons with the porous material.[63,64] A positron annihilates when it meets an electron inside the material and emits gamma rays outward. Within material containing pores, the positron can form a positron–electron bound state called positronium (Ps). Ps exists as *para*-Ps (*p*-Ps, singlet state) and *ortho*-Ps (*o*-Ps, triplet state) with a lifetime in vacuum of 125 ps and 142 ns, respectively. The *p*-Ps has a self-annihilation process with a very short lifetime. In
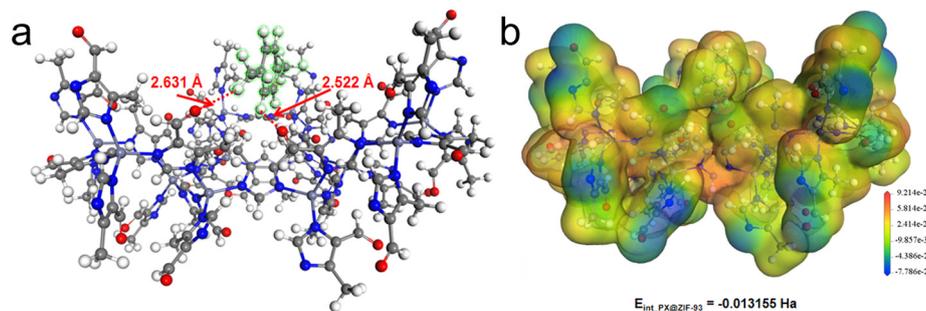

Fig. 8 (a) Adsorption sites and (b) electrostatic potential of *p*-xylene on ZIF-93.
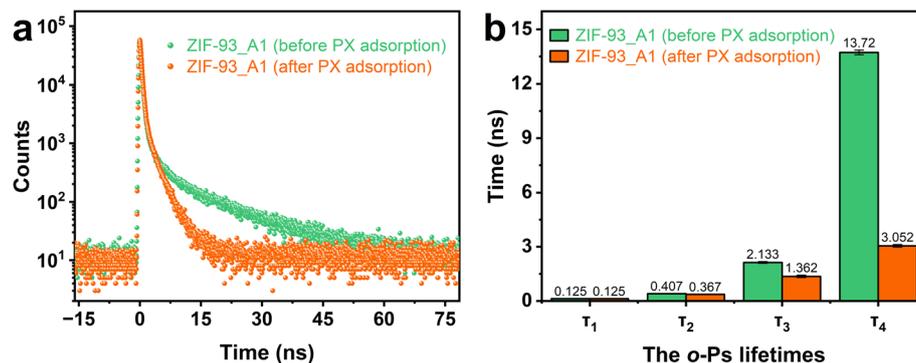
Fig. 9 (a) Peak-normalized positron lifetime spectrum and (b) *o*-Ps lifetimes for ZIF-93_A1 before and after adsorption of *p*-xylene.

contrast, *o*-Ps annihilate only when they encounter electrons of opposite spin in the surrounding environment, the process known as "pick-off annihilation". The pick-off lifetime of *o*-Ps is related to the pore size: the larger the pore, the longer the pick-off lifetime.[65]

Fig. 9 shows the peak-normalized positron lifetime spectrum and *o*-Ps lifetimes analysis results for ZIF-93. As shown in Fig. 9a, the intensity of the longest lifetime component of *o*-Ps decreases significantly after adsorption of *p*-xylene. From Fig. 9b, the shortest lifetime τ_1 (0.125 ns) is defined as the self-annihilation of *p*-Ps and the annihilation lifetime of free positrons. This data does not contain any important information about the pore structure of the framework and is therefore not repeated. The second lifetime τ_2 is due to annihilation of positrons at open volume defects on the surface. The decrease in τ_2 after adsorption of *p*-xylene indicates that a small amount of *p*-xylene was adsorbed at the defects on the surface of ZIF-93. The long lifetimes of τ_3 and τ_4 indicate the annihilation of positrons at the micropores and mesopores of the ZIF-93, respectively. Therefore, τ_3 and τ_4 can reflect the porosity information of ZIF-93.[66] The significant shortening of τ_3 and τ_4 after the adsorption of *p*-xylene indicated that *p*-xylene was adsorbed in the inner part of the pore channels, proving the connectivity of micropore-mesopore-macropores in the hierarchically porous ZIF-93.

Tao and Eldrup proposed a semi-empirical equation (eqn (1)), which gives a relationship between the lifetime of *o*-Ps and the average radius of spherical pores (*R*).[64]

$$\frac{1}{\tau_{o\text{-Ps}}} = 2\left[1 - \frac{R}{R + \Delta R} + \frac{1}{2\pi}\sin\left(2\pi\frac{R}{R + \Delta R}\right)\right] \quad (1)$$

where the parameter ΔR = 0.1656 nm is a constant, representing the thickness of the electron layer at the pore wall.

According to eqn (1), the average diameter of micropores corresponding to the long lifetime τ_3 of ZIF-93_A1 is 0.30 nm. Compared to the microporous pore size measured by CO_2 adsorption (0.40 nm) is smaller and more realistic.

However, the Tao–Eldrup model is only applicable to micropores with a radius less than 1 nm. As the pore diameter increases, the probability of collision between the

electron dipole and the pore surface becomes smaller, and some *o*-Ps undergo self-annihilation with a long lifetime of 142 ns. The Tao–Eldrup model does not consider the self-annihilation of *o*-Ps. To obtain the size of the mesopores from the *o*-Ps lifetime, many researchers have extended the Tao–Eldrup model by considering the influence of the self-annihilation of *o*-Ps. Ito *et al.*[67] proposed a modified model taking into account the self-annihilation of *o*-Ps as follows:

$$\frac{1}{\tau_{o\text{-Ps}}} = 2\left[1 - \frac{R_a}{R_a + \Delta R} + \frac{1}{2\pi}\sin\left(2\pi\frac{R_a}{R_a + \Delta R}\right)\right]\left[1 - \left(\frac{R - R_a}{R + \Delta R}\right)^b\right] + \frac{1}{142}$$

(2)

where R_a = 0.88 nm and b = 0.55 are the two fitting parameters and the last 1/142 term is the self-annihilation rate of the *o*-Ps.[67]

According to eqn (2), the mesopore diameter corresponding to the long lifetime τ_4 of ZIF-93_A1 is 3.12 nm.

3 Conclusions

In summary, hierarchically porous ZIF-93 (ZIF-93_A*t*) was synthesized using a simple, rapid, and versatile method with an alkali (NaOH, KOH, and $NH_3\cdot H_2O$) as a deprotonating agent. The facile synthesis conditions were room temperature and water-based with a short synthesis time of 1 min. The as-synthesized ZIF-93_A*t* showed three types of pores, with mesopores and macropores interconnected with micropores, and exhibited good thermal and water stability. The space–time yield (STY) of hierarchically porous ZIF-93 (9670 kg m^{-3} d^{-1}) is 712 times higher than previously reported results, which is significant for the large-scale preparation of HP-ZIFs. The porosities of the HP-ZIFs can be readily tuned by varying the reaction time, ratios, metal source, and alkali source. The as-synthesized ZIF-93_A1 demonstrated improved capacities for capturing VOCs compared to conventional ZIF-93 due to the introduction of mesopores and macropores. Furthermore, the pore connectivity of HP-ZIF was investigated using advanced techniques such as positron annihilation lifetime spectroscopy (PALS). Molecular simulations were used to elucidate the adsorption behaviour

of VOCs in HP-ZIFs. The integration of environmental friendliness, hierarchical pores, and large-scale productive potential implies that these HP-ZIFs are high-potential porous platforms for a wide range of applications.

4 Experimental section

4.1 Materials

Zinc acetate dihydrate ($Zn(OAc)_2 \cdot 2H_2O$, 99.99%, Macklin), zinc sulfate heptahydrate ($ZnSO_4 \cdot 7H_2O$, 99.5%, Macklin), zinc nitrate hexahydrate ($Zn(NO_3)_2 \cdot 6H_2O$, 99%, Aladdin Chemical Ltd), 4-methylimidazole-5-carbaldehyde ($C_5H_6N_2O$, 99%, Aladdin Chemical Ltd), N,N-dimethylformamide (DMF, 99.5%, Macklin), sodium hydroxide (NaOH, AR, Macklin), potassium hydroxide (KOH, AR, Macklin), ammonium hydroxide solution ($NH_3 \cdot H_2O$, AR, JDTZ Chemical Reagent Factory), methanol (CH_3OH, 99.5%, Macklin), p-xylene (C_8H_{10}, AR, Aladdin Chemical Ltd), n-hexane (C_6H_{14}, AR, Aladdin Chemical Ltd), deionized water (laboratory homemade). The above chemical reagents were used without further purification.

4.2 Synthesis of hierarchically porous ZIF-93

Typically, 988 mg of $Zn(OAc)_2 \cdot 2H_2O$ and 991 mg of 4-methylimidazole-5-carbaldehyde (almeIm) were dissolved in 225 mL of deionized water, then 162 mg of NaOH was added to the above solution while stirring rapidly (2000 rpm). The final molar ratio was Zn^{2+}/almeIm/NaOH/H_2O = 1/2/0.9/2780. Then stirred at room temperature for t (t = 1, 10, 60) min, after the product was collected by centrifugation (10 000 rpm, 10 min) and washed three times with methanol under the same centrifugation program, the product was dried overnight in a vacuum oven at room temperature. The resulting products were denoted as ZIF-93_At (t = 1, 10, 60, corresponding to reaction times t = 1, 10, 60 min, respectively).

To explore the effect of activation on the hierarchically porous structures of ZIF-93_At, the activated-ZIF-93 sample was synthesized according to the same molar ratio and synthesis steps as above (only adding the step of activation with methanol at 60 °C for 12 h after washing). To explore the influence of other bases ($NH_3 \cdot H_2O$, KOH) and other zinc sources ($ZnSO_4$, $Zn(NO_3)_2$) on ZIF-93 materials, a series of ZIF-93 samples were synthesized according to the same molar ratio and synthesis steps as above. To explore the effect of different molar ratios on ZIF-93 materials. A series of ZIF-93 samples were synthesized by following the same synthesis procedure described above, varying only the molar ratios of Zn^{2+}/almeIm and Zn^{2+}/H_2O. It is worth noting that the synthesis time of the above additional experiments is 1 min.

4.3 Synthesis of conventional ZIF-93

Typically,[58] 176 mg of $Zn(OAc)_2 \cdot 2H_2O$ and 264 mg of almeIm were dissolved in 16 ml of N,N-dimethylformamide (DMF) in a 30 mL Teflon-lined autoclave. The sealed autoclave was heated in an oven at 85 °C for 12 h. After the reaction was completed, the crystalline powder was collected by centrifugation at 10 000 rpm for 10 min and washed three times with methanol through the same centrifugation procedure. The product was activated with methanol over three days before drying under a vacuum oven for 24 h at 80 °C. The obtained product was denoted as C-ZIF-93.

4.4 Characterization

Power X-ray diffraction (XRD) patterns were recorded on a TD-3500 (TongDa, China) using a step scan model with a range of 3–40° with Ni-filtered Cu-target Kα radiation (30 kV, 20 mA, wavelength λ = 0.15418 nm). Fourier transform infrared (FT-IR) spectra were measured using a Vector 33 (Bruker, Germany) spectrometer with a resolution of 4 cm^{-1}. N_2 adsorption–desorption data were measured on an ASAP 2460 (Micromeritics) system at 77 K. CO_2 adsorption–desorption data were measured on an ASAP 2020 (Micromeritics) system at 273 K. Scanning electron microscope (SEM) images were obtained on a HITACHI (SC8820, Japan). Transmission electron microscopy (TEM) images were obtained using a JEM-2100HR (JEOL, Japan). Thermogravimetry (TGA) was performed by a TGA 2 instrument (METTLER TOLEDO) between 30 °C and 900 °C at a heating rate of 10 K min^{-1} in a N_2 atmosphere. Gaseous p-xylene and n-hexane adsorption experiments were performed on a vacuum vapor/gas sorption analyzer (BSD-VVS, BeiShiDe Instruments Technology (Beijing) Co., Ltd.), ZIF-93 samples were outgassed for 6 h at 120 °C before the test. Positron annihilation lifetime spectroscopy (PALS) tests are described in more detail in our previous work.[68]

4.5 Simulation details

The adsorption density of p-xylene and n-hexane on ZIF-93 was calculated by grand canonical Monte Carlo (GCMC) simulations with the RASPA 2.0.2 package. The structure of ZIF-93 was taken from the Cambridge Crystallographic Data Centre (CCDC: 1951993).[58] GCMC calculations were done through the sorption module in the Materials Studio software to simulate the adsorption of p-xylene and n-hexane at different pressures of 298 K. The configurational bias method in the adsorption isotherm task was used with the accuracy set to ultra-fine, 5×10^6 Monte Carlo for equilibrating the system in the first part of the calculation and 5×10^6 Monte Carlo for statistical averaging in the second part, and the force field was adopted from Universal, through the QEq method for assigning charges to the system, and Ewald and Atom based summation methods for electrostatic and van der Waals interactions, respectively. Adsorption site analysis was performed by locate task to obtain the adsorption configuration. For each adsorption density model, 1000 snapshots were stacked to show the distribution of adsorbates in the framework pores.

Data availability

The data that support the findings of this study are available from the corresponding author, Prof. Duan, upon reasonable request.

Conflicts of interest

The authors declare no conflict of interest.

Acknowledgements

References

1 M. R. Saleh, H. M. El-Bery and H. N. Abdelhamid, Co@ZIF-8/TiO₂ heterojunction for green hydrogen generation, *Appl. Organomet. Chem.*, 2023, **37**, e6995.

2 Y. W. Abraha, C.-W. Tsai and E. H. G. Langner, Scalable synthesis of mixed-linker (Zn) ZIFs and their application in CO₂ adsorption and fixation, *J. Porous Mater.*, 2023, **30**, 149–162.

3 M. Thommes, K. Kaneko, A. V. Neimark, J. P. Olivier, F. Rodriguez-Reinoso, J. Rouquerol and K. S. W. Sing, Physisorption of gases, with special reference to the evaluation of surface area and pore size distribution (IUPAC technical report), *Pure Appl. Chem.*, 2015, **87**, 1051–1069.

4 C. Duan, F. Li, M. Yang, H. Zhang, Y. Wu and H. Xi, Rapid synthesis of hierarchically structured multifunctional metal–organic zeolites with enhanced volatile organic compounds adsorption capacity, *Ind. Eng. Chem. Res.*, 2018, **57**, 15385–15394.

5 X. Qian, Q. Ren, X. Wu, J. Sun, H. Wu and J. Lei, Enhanced water stability in Zn-doped zeolitic imidazolate framework-67 (ZIF-67) for CO₂ capture applications, *ChemistrySelect*, 2018, **3**, 657–661.

6 Z. Zhang, Y. Chen, C. Hu, C. Zuo, P. Wang, W. Chen and T. Ao, Efficient removal of tetracycline by a hierarchically porous ZIF-8 metal organic framework, *Environ. Res.*, 2021, **198**, 111254.

7 Y. Sun, N. Zhang, Y. Yue, J. Xiao, X. Huang and A. Ishag, Recent advances in the application of zeolitic imidazolate frameworks (ZIFs) in environmental remediation: A review, *Environ. Sci.: Nano*, 2022, **9**, 4069–4092.

8 H. Park, D. Amaranatha Reddy, Y. Kim, R. Ma, J. Choi, T. K. Kim and K.-S. Lee, Zeolitic imidazolate framework-67 (ZIF-67) rhombic dodecahedrons as full-spectrum light harvesting photocatalyst for environmental remediation, *Solid State Sci.*, 2016, **62**, 82–89.

9 H. N. Abdelhamid, Zeolitic imidazolate frameworks (ZIF-8) for biomedical applications: A review, *Curr. Med. Chem.*, 2021, **28**, 7023–7075.

10 B. Ding, H. Chen, J. Tan, Q. Meng, P. Zheng, P. A. Ma and J. Lin, ZIF-8 nanoparticles evoke pyroptosis for high-efficiency cancer immunotherapy, *Angew. Chem.*, 2023, **62**, e202215307.

11 K. Shen, X. Chen, J. Chen and Y. Li, Development of MOF-derived carbon-based nanomaterials for efficient catalysis, *ACS Catal.*, 2016, **6**, 5887–5903.

12 A. Shahzad, F. Zulfiqar and M. Arif Nadeem, Cobalt containing bimetallic ZIFs and their derivatives as OER electrocatalysts: A critical review, *Coord. Chem. Rev.*, 2023, **477**, 214925.

13 H. Deng, S. Grunder, K. E. Cordova, C. Valente, H. Furukawa, M. Hmadeh, F. Gándara, A. C. Whalley, Z. Liu, S. Asahina, H. Kazumori, M. O'Keeffe, O. Terasaki, J. F. Stoddart and O. M. Yaghi, Large-pore apertures in a series of metal-organic frameworks, *Science*, 2012, **336**, 1018–1023.

14 X. Chen, X. Jiang, C. Yin, B. Zhang and Q. Zhang, Facile fabrication of hierarchical porous ZIF-8 for enhanced adsorption of antibiotics, *J. Hazard. Mater.*, 2019, **367**, 194–204.

15 C. Duan, J. Huo, F. Li, M. Yang and H. Xi, Ultrafast room-temperature synthesis of hierarchically porous metal–organic frameworks by a versatile cooperative template strategy, *J. Mater. Sci.*, 2018, **53**, 16276–16287.

16 K. Shen, L. Zhang, X. Chen, L. Liu, D. Zhang, Y. Han, J. Chen, J. Long, R. Luque, Y. Li and B. Chen, Ordered macro-microporous metal-organic framework single crystals, *Science*, 2018, **359**, 206–210.

17 H. Cao, S. Wang, Y. Wang, H. Lyu, R. Krishna, Z. Lu, J. Duan and W. Jin, Pre-design and synthesis of a five-fold interpenetrated pcu-type porous coordination polymer and its CO₂/CO separation, *CrystEngComm*, 2017, **19**, 6927–6931.

18 W. Yao, C. Hu, Y. Zhang, H. Li, F. Wang, K. Shen, L. Chen and Y. Li, Hierarchically ordered porous carbon with atomically dispersed cobalt for oxidative esterification of furfural, *Ind. Chem. Mater.*, 2023, **1**, 106–116.

19 L. Song, J. Zhang, L. Sun, F. Xu, F. Li, H. Zhang, X. Si, C. Jiao, Z. Li, S. Liu, Y. Liu, H. Zhou, D. Sun, Y. Du, Z. Cao and Z. Gabelica, Mesoporous metal–organic frameworks: Design and applications, *Energy Environ. Sci.*, 2012, **5**, 7508–7520.

20 C. Duan, Y. Yu, P. Yang, X. Zhang, F. Li, L. Li and H. Xi, Engineering new defects in MIL-100(Fe) via a mixed-ligand approach to effect enhanced volatile organic compound adsorption capacity, *Ind. Eng. Chem. Res.*, 2020, **59**, 774–782.

21 G. Cai and H.-L. Jiang, A modulator-induced defect-formation strategy to hierarchically porous metal–organic frameworks with high stability, *Angew. Chem., Int. Ed.*, 2017, **56**, 563–567.

© 2025 The Author(s). Co-published by the Institute of Process Engineering, Chinese Academy of Sciences and the Royal Society of Chemistry

Ind. Chem. Mater., 2025, **3**, 109–121 | 119

22 M. Yin, Z. Li, L. Wang and S. Tang, Preparation of hierarchically porous PVP/ZIF-8 in supercritical CO_2 by PVP-induced defect-formation method for high-efficiency gas adsorption, *Sep. Purif. Technol.*, 2023, **314**, 123550.

23 C. Duan, Y. Yu, J. Xiao, X. Zhang, L. Li, P. Yang, J. Wu and H. Xi, Water-based routes for synthesis of metal-organic frameworks: A review, *Sci. China Mater.*, 2020, **63**, 667–685.

24 H. Zhang, C. Duan, F. Li, X. Yan and H. Xi, Green and rapid synthesis of hierarchical porous zeolitic imidazolate frameworks for enhanced CO_2 capture, *Inorg. Chim. Acta*, 2018, **482**, 358–363.

25 M. Jian, B. Liu, R. Liu, J. Qu, H. Wang and X. Zhang, Water-based synthesis of zeolitic imidazolate framework-8 with high morphology level at room temperature, *RSC Adv.*, 2015, **5**, 48433–48441.

26 E. V. Ramos-Fernandez, A. Redondo-Murcia, A. Grau-Atienza, A. Sepúlveda-Escribano and J. Narciso, Clean production of zeolitic imidazolate framework 8 using zamak residues as metal precursor and substrate, *J. Cleaner Prod.*, 2020, **260**, 121081.

27 J. J. Delgado-Marín, D. P. Izan, M. Molina-Sabio, E. V. Ramos-Fernandez and J. Narciso, New generation of MOF-monoliths based on metal foams, *Molecules*, 2022, **27**, 1968.

28 Y. Yu, Z. Liu, X. Chen, S. Liu, C. Duan and H. Xi, Water-based synthesis of nanoscale hierarchical metal-organic frameworks: boosting adsorption and catalytic performance, *Nano Mater. Sci.*, 2023, **5**, 361–368.

29 E. V. Ramos-Fernandez, A. Grau-Atienza, D. Farrusseng and S. Aguado, A water-based room temperature synthesis of ZIF-93 for CO_2 adsorption, *J. Mater. Chem. A*, 2018, **6**, 5598–5602.

30 K. Kida, M. Okita, K. Fujita, S. Tanaka and Y. Miyake, Formation of high crystalline ZIF-8 in an aqueous solution, *CrystEngComm*, 2013, **15**, 1794–1801.

31 Y. Ding, H. Wang, M. Yu, W. Zheng, X. Ruan, X. Li, Y. Xi, Y. Dai, H. Liu and G. He, Amine group graft ZIF-93 to create gas storage space to improve the gas separation performance of pebax-1657 MMMs, *Sep. Purif. Technol.*, 2022, **309**, 122949.

32 V. Berned-Samatán, C. Rubio, A. Galán-González, E. Muñoz, A. M. Benito, W. K. Maser, J. Coronas and C. Téllez, Single-walled carbon nanotube buckypaper as support for highly permeable double layer polyamide/zeolitic imidazolate framework in nanofiltration processes, *J. Membr. Sci.*, 2022, **652**, 120490.

33 V. Berned-Samatán, M. Piantek, J. Coronas and C. Téllez, Nanofiltration with polyamide thin film composite membrane with ZIF-93/SWCNT intermediate layers on polyimide support, *Sep. Purif. Technol.*, 2023, **308**, 122915.

34 L. Paseta, D. Antorán, J. Coronas and C. Téllez, 110th anniversary: Polyamide/metal–organic framework bilayered thin film composite membranes for the removal of pharmaceutical compounds from water, *Ind. Eng. Chem. Res.*, 2019, **58**, 4222–4230.

35 L. Paseta, M. Navarro, J. Coronas and C. Téllez, Greener processes in the preparation of thin film nanocomposite membranes with diverse metal-organic frameworks for organic solvent nanofiltration, *J. Ind. Eng. Chem.*, 2019, **77**, 344–354.

36 H. Ghaedrahmat, M. Y. Masoomi and M. Zendehdel, Synthesize and characterization of ZIF-8/NaP zeolite composites as a stable acid-base catalyst for organic reactions, *Polyhedron*, 2023, **236**, 116372.

37 E. Aliyev, J. Warfsmann, B. Tokay, S. Shishatskiy, Y.-J. Lee, J. Lillepaerg, N. R. Champness and V. Filiz, Gas transport properties of the metal–organic framework (MOF)-assisted polymer of intrinsic microporosity (PIM-1) thin-film composite membranes, *ACS Sustainable Chem. Eng.*, 2021, **9**, 684–694.

38 Z. Lyu, G. J. H. Lim, R. Guo, Z. Kou, T. Wang, C. Guan, J. Ding, W. Chen and J. Wang, 3D-printed MOF-derived hierarchically porous frameworks for practical high-energy density Li–O_2 batteries, *Adv. Funct. Mater.*, 2019, **29**, 1806658.

39 Y. Yao, X. Zhao, G. Chang, X. Yang and B. Chen, Hierarchically porous metal–organic frameworks: Synthetic strategies and applications, *Small Struct.*, 2023, **4**, 2200187.

40 S. Øien-Ødegaard, G. C. Shearer, D. S. Wragg and K. P. Lillerud, Pitfalls in metal–organic framework crystallography: towards more accurate crystal structures, *Chem. Soc. Rev.*, 2017, **46**, 4867–4876.

41 C. Duan, F. Li, H. Zhang, J. Li, X. Wang and H. Xi, Template synthesis of hierarchical porous metal–organic frameworks with tunable porosity, *RSC Adv.*, 2017, **7**, 52245–52251.

42 E. V. Perez, K. J. Balkus, J. P. Ferraris and I. H. Musselman, Mixed-matrix membranes containing MOF-5 for gas separations, *J. Membr. Sci.*, 2009, **328**, 165–173.

43 C. Healy, K. M. Patil, B. H. Wilson, L. Hermanspahn, N. C. Harvey-Reid, B. I. Howard, C. Kleinjan, J. Kolien, F. Payet, S. G. Telfer, P. E. Kruger and T. D. Bennett, The thermal stability of metal-organic frameworks, *Coord. Chem. Rev.*, 2020, **419**, 213388.

44 S. Wang and S. Zhang, Study on the structure activity relationship of ZIF-8 synthesis and thermal stability, *J. Inorg. Organomet. Polym. Mater.*, 2017, **27**, 1317–1322.

45 K. S. Park, Z. Ni, A. P. Côté, J. Y. Choi, R. Huang, F. J. Uribe-Romo, H. K. Chae, M. O'Keeffe and O. M. Yaghi, Exceptional chemical and thermal stability of zeolitic imidazolate frameworks, *Proc. Natl. Acad. Sci. U. S. A.*, 2006, **103**, 10186–10191.

46 S. H. Madani, C. Hu, A. Silvestre-Albero, M. J. Biggs, F. Rodríguez-Reinoso and P. Pendleton, Pore size distributions derived from adsorption isotherms, immersion calorimetry, and isosteric heats: A comparative study, *Carbon*, 2016, **96**, 1106–1113.

47 S. Dantas, K. C. Struckhoff, M. Thommes and A. V. Neimark, Pore size characterization of micro-mesoporous carbons using CO_2 adsorption, *Carbon*, 2021, **173**, 842–848.

48 N. D. Hutson and R. T. Yang, Theoretical basis for the Dubinin-Radushkevitch (D-R) adsorption isotherm equation, *Adsorption*, 1997, **3**, 189–195.

49 M. Heuchel, D. Fritsch, P. M. Budd, N. B. McKeown and D. Hofmann, Atomistic packing model and free volume distribution of a polymer with intrinsic microporosity (PIM-1), *J. Membr. Sci.*, 2008, **318**, 84–99.

50 J. E. Mondloch, O. Karagiaridi, O. K. Farha and J. T. Hupp, Activation of metal–organic framework materials, *CrystEngComm*, 2013, **15**, 9258–9264.

51 X. Zhang, Z. Chen, X. Liu, S. L. Hanna, X. Wang, R. Taheri-Ledari, A. Maleki, P. Li and O. K. Farha, A historical overview of the activation and porosity of metal–organic frameworks, *Chem. Soc. Rev.*, 2020, **49**, 7406–7427.

52 X. Liu, Y. Li, Y. Ban, Y. Peng, H. Jin, W. Yang and K. Li, Synthesis of zeolitic imidazolate framework nanocrystals, *Mater. Lett.*, 2014, **136**, 341–344.

53 D. Madhav, M. Malankowska and J. Coronas, Synthesis of nanoparticles of zeolitic imidazolate framework ZIF-94 using inorganic deprotonators, *New J. Chem.*, 2020, **44**, 20449–20457.

54 K. Kenyotha, K. C. Chanapattharapol, S. McCloskey and P. Jantaharn, Water based synthesis of ZIF-8 assisted by hydrogen bond acceptors and enhancement of CO_2 uptake by solvent assisted ligand exchange, *Crystals*, 2020, **10**, 599.

55 J. Yao, M. He, K. Wang, R. Chen, Z. Zhong and H. Wang, High-yield synthesis of zeolitic imidazolate frameworks from stoichiometric metal and ligand precursor aqueous solutions at room temperature, *CrystEngComm*, 2013, **15**, 3601–3606.

56 M. Rubio-Martinez, C. Avci-Camur, A. W. Thornton, I. Imaz, D. Maspoch and M. R. Hill, New synthetic routes towards MOF production at scale, *Chem. Soc. Rev.*, 2017, **46**, 3453–3480.

57 P. Silva, S. M. F. Vilela, J. P. C. Tomé and F. A. A. Paz, Multifunctional metal–organic frameworks: from academia to industrial applications, *Chem. Soc. Rev.*, 2015, **44**, 6774–6803.

58 W. Morris, B. Leung, H. Furukawa, O. K. Yaghi, N. He, H. Hayashi, Y. Houndonougbo, M. Asta, B. B. Laird and O. M. Yaghi, A combined experimental–computational investigation of carbon dioxide capture in a series of isoreticular zeolitic imidazolate frameworks, *J. Am. Chem. Soc.*, 2010, **132**, 11006–11008.

59 M. Jahandar Lashaki, M. Fayaz, S. Niknaddaf and Z. Hashisho, Effect of the adsorbate kinetic diameter on the accuracy of the Dubinin–Radushkevich equation for modeling adsorption of organic vapors on activated carbon, *J. Hazard. Mater.*, 2012, **241–242**, 154–163.

60 L. Figueroa-Quintero, E. V. Ramos-Fernandez and J. Narciso, Synthesis and characterization of the metal–organic framework CIM-80 for organic compounds adsorption, *Materials*, 2022, **15**, 5326.

61 K. G. Ray, D. L. Olmsted, J. M. R. Burton, Y. Houndonougbo, B. B. Laird and M. Asta, Gas membrane selectivity enabled by zeolitic imidazolate framework electrostatics, *Chem. Mater.*, 2014, **26**, 3976–3985.

62 B. Siu, A. R. Chowdhury, Z. Yan, S. M. Humphrey and T. Hutter, Selective adsorption of volatile organic compounds in metal-organic frameworks (MOFs), *Coord. Chem. Rev.*, 2023, **485**, 215119.

63 S. J. Tao, Positronium annihilation in molecular substances, *J. Chem. Phys.*, 1972, **56**, 5499–5510.

64 M. Eldrup, D. Lightbody and J. N. Sherwood, The temperature dependence of positron lifetimes in solid pivalic acid, *Chem. Phys.*, 1981, **63**, 51–58.

65 T. Stassin, R. Verbeke, A. J. Cruz, S. Rodríguez-Hermida, I. Stassen, J. Marreiros, M. Krishtab, M. Dickmann, W. Egger, I. F. J. Vankelecom, S. Furukawa, D. De Vos, D. Grosso, M. Thommes and R. Ameloot, Porosimetry for thin films of metal–organic frameworks: a comparison of positron annihilation lifetime spectroscopy and adsorption-based methods, *Adv. Mater.*, 2021, **33**, 2006993.

66 S. K. Sharma and P. K. Pujari, Role of free volume characteristics of polymer matrix in bulk physical properties of polymer nanocomposites: a review of positron annihilation lifetime studies, *Prog. Polym. Sci.*, 2017, **75**, 31–47.

67 K. Ito, H. Nakanishi and Y. Ujihira, Extension of the equation for the annihilation lifetime of ortho-positronium at a cavity larger than 1 nm in radius, *J. Phys. Chem. B*, 1999, **103**, 4555–4558.

68 X. Zhang, L. Qian, S. Yang, Y. Peng, B. Xiong, J. Li, P. Fang and C. He, Comparative studies of methyl orange adsorption in various metal-organic frameworks by nitrogen adsorption and positron annihilation lifetime spectroscopy, *Microporous Mesoporous Mater.*, 2020, **296**, 109993.

© 2025 The Author(s). Co-published by the Institute of Process Engineering, Chinese Academy of Sciences and the Royal Society of Chemistry

Ind. Chem. Mater., 2025, **3**, 109–121 | **121**